Eur J Nucl Med Mol Imaging (2010) 37:1539–1550
DOI 10.1007/s00259-010-1443-z

ORIGINAL ARTICLE

Image-derived input function in dynamic human PET/CT: methodology and validation with ^{11}C-acetate and ^{18}F-fluorothioheptadecanoic acid in muscle and ^{18}F-fluorodeoxyglucose in brain

Etienne Croteau · Éric Lavallée · Sébastien M. Labbe · Laurent Hubert · Fabien Pifferi · Jacques A. Rousseau · Stephen C. Cunnane · André C. Carpentier · Roger Lecomte · François Bénard

Received: 25 November 2009 / Accepted: 8 March 2010 / Published online: 2 May 2010

Abstract
Purpose Despite current advances in PET/CT systems, blood sampling still remains the standard method to obtain the radiotracer input function for tracer kinetic modelling. The purpose of this study was to validate the use of image-derived input functions (IDIF) of the carotid and femoral arteries to measure the arterial input function (AIF) in PET imaging. The data were obtained from two different research studies, one using ^{18}F-FDG for brain imaging and the other using ^{11}C-acetate and ^{18}F-fluoro-6-thioheptadecanoic acid (^{18}F-FTHA) in femoral muscles.
Methods The method was validated with two phantom systems. First, a static phantom consisting of syringes of different diameters containing radioactivity was used to determine the recovery coefficient (RC) and spill-in factors. Second, a dynamic phantom built to model bolus injection and clearance of tracers was used to establish the correlation between blood sampling, AIF and IDIF. The RC was then applied to the femoral artery data from PET imaging studies with ^{11}C-acetate and ^{18}F-FTHA and to carotid artery data from brain imaging with ^{18}F-FDG. These IDIF data were then compared to actual AIFs from patients.
Results With ^{11}C-acetate, the perfusion index in the femoral muscle was 0.34±0.18 min^{-1} when estimated from the actual time–activity blood curve, 0.29±0.15 min^{-1} when estimated from the corrected IDIF, and 0.66±0.41 min^{-1} when the IDIF data were not corrected for RC. A one-way repeated measures (ANOVA) and Tukey's test showed a statistically significant difference for the IDIF not corrected for RC ($p<0.0001$). With ^{18}F-FTHA there was a strong correlation between Patlak slopes, the plasma to tissue transfer rate calculated using the true plasma radioactivity content and the corrected IDIF for the femoral muscles (vastus lateralis $r=0.86$, $p=0.027$; biceps femoris r=0.90, $p=0.017$). On the other hand, there was no correlation between the values derived using the AIF and those derived using the uncorrected IDIF. Finally, in the brain imaging

E. Croteau · É. Lavallée · L. Hubert · J. A. Rousseau · R. Lecomte
Department of Nuclear Medicine and Radiobiology, Faculty of Medicine and Health Sciences, Université de Sherbrooke, Sherbrooke, QC, Canada

E. Croteau · É. Lavallée · L. Hubert · J. A. Rousseau · R. Lecomte
Sherbrooke Molecular Imaging Center, Centre de recherche clinique Étienne-LeBel, Centre Hospitalier Universitaire de Sherbrooke, Sherbrooke, QC, Canada

F. Pifferi · S. C. Cunnane
Research Center on Aging, Université de Sherbrooke, Sherbrooke, QC, Canada

S. M. Labbe · S. C. Cunnane · A. C. Carpentier
Department of Medicine, Centre Hospitalier Universitaire de Sherbrooke, Sherbrooke, QC, Canada

F. Pifferi
Mécanismes Adaptatifs et Évolution, MNHN-CNRS, Brunoy, France

F. Bénard
Division of Nuclear Medicine, Department of Radiology, University of British Columbia, Vancouver, BC, Canada

F. Bénard (✉)
BC Cancer Agency, 675 West 10th Avenue, Vancouver, BC V5Z 1L3, Canada
e-mail: fbenard@bccrc.ca

study with ^{18}F-FDG, the cerebral metabolic rate of glucose (CMRglc) measured using the uncorrected IDIF was consistently overestimated. The CMRglc obtained using blood sampling was 13.1±3.9 mg/100 g per minute and 14.0±5.7 mg/100 g per minute using the corrected IDIF (r^2=0.90).

Conclusion Correctly obtained, carotid and femoral artery IDIFs can be used as a substitute for AIFs to perform tracer kinetic modelling in skeletal femoral muscles and brain analyses.

Keywords Positron emission tomography · Tracer kinetic modelling · Image-derived input function

Abbreviation

AIF	Arterial input function
CMRglc	Cerebral metabolic rate of glucose
FDG	Fluorodeoxyglucose
FTHA	Fluorothioheptadecanoic acid
IDIF	Image-derived input function
PVE	Partial volume effect
RC	Recovery coefficient
ROI	Region of interest
TAC	Time–activity curve

Introduction

PET is an important tool to probe in vivo biochemistry and metabolism for cardiac, brain and cancer imaging [1]. This has prompted the development of several new radiotracers and imaging techniques, including tracer kinetic modelling methods to quantify various physiological or biochemical parameters [2–4]. While diagnostic studies in oncology commonly use the semiquantitative standardized uptake value, a single static measurement [5, 6], metabolic research questions generally require more complex tracer kinetic modelling approaches or graphical analysis [1, 7, 8]. Tracer kinetics can be used to model specific physiological or biochemical parameters and to decouple the various factors involved in tracer influx and efflux from a tissue [5, 9–12].

The most common kinetic models are compartmental kinetic models [5, 13] and graphical analysis methods such as the Patlak plot, also called the Gjedde-Patlak and Patlak-Rutland plot [1, 14]. Both approaches require an accurate estimation of the arterial input function (AIF), for which multiple samples of arterial blood or arterialized venous blood are needed [15, 16]. Arterial access can be problematic in some patients and has a low but still significant risk of complications [8, 9]. Venous access in the hand to obtain arterialized venous blood can be difficult and it is not always possible to maintain consistent sampling, timing and volume across experiments. Multiple blood sampling requires additional staff and may be more difficult in the clinical setting or in large-scale studies.

Alternatives to multiple blood sampling exist, including general population standard curves [17] or reduction of the number of blood samples [4, 8]. Indeed, in some situations, only one blood sample may be sufficient [9]. A reference tissue region of interest (ROI) such as muscle can sometimes be used to eliminate the need for an AIF [18], but in many cases such an ROI may not be available. Factorial analysis which targets well-defined parameters to which the proper kinetic function is attributed has also been used [3].

Accurate image-derived input functions (IDIF) obtained from dynamic images would greatly simplify tracer kinetic modelling or graphical methods in quantitative clinical PET studies. Since large arteries are often in the same field of view as the target organ of interest, in principle, the AIF can be obtained directly from imaging data, much as is done in cardiac imaging using the myocardial cavity [2]. Indeed, the use of carotid arteries to obtain the IDIF for brain studies has already been explored by several groups [8, 19–23] showing that with proper correction for partial volume effect (PVE), IDIF can be a suitable alternative to AIF.

Hence, the purpose of the present study was to thoroughly validate the use of the IDIF and calculate suitable factors for PVE correction of an artery's diameter. This was done using two different phantoms to mimic blood vessels of various sizes and to model the AIF. Our human data came from studies performed on two different scanners, a Gemini GXL scanner [24] and a Gemini TF "time of flight" PET/CT scanner [25], so the validation was done for both scanners taking into account the properties of each and the nature of the radioisotopes. We then applied the derived correction factors to two human PET/CT studies in which AIFs had been obtained from arterialized venous blood samples.

Material and methods

Phantoms

Two different phantoms were used to develop our IDIF method, one to validate the measurement of radioactivity as a function of arterial diameter, including PVE and spill-in effect, and the other to simulate the kinetics of a bolus tracer injection into the arterial system. The first phantom consisted of six syringes ranging in diameter from 4.7 to 29 mm (1 to 60 cm^3). These syringes were immersed in a Plexiglas cylinder (diameter 19.9 cm, length 30 cm) filled with water to represent the attenuation and scattering environment of the patient. Artery size and IDIF phantom

studies were repeated for both the Philips Gemini GXL scanner and the Philips Gemini TF scanner with [^{11}C] and [^{18}F] at a concentration of 0.07±0.03 MBq/ml using the same acquisition parameters as for the human studies (see below). The spill-in factors were calculated using cold syringes immersed in a radioactive water cylinder ranging between 6.0 and 1.0 kBq/ml for the representation of muscle radioactivity contamination.

The first aim of the static phantom study was to determine the recovery correction factors as a function of object diameter for each scanner [26] (Fig. 1). Briefly, once the images were reconstructed, three ROIs were drawn on each syringe in the transaxial planes, and then for each ROI the maximum value of the four highest adjacent pixels was recorded and fitted to Eq. 1 to obtain the recovery coefficient (RC) as a function of object diameter x (Fig. 1a).

$$RC(x) = a \cdot (x-d)/(1+((x-d)/b)^c)^{1/c} \quad (1)$$

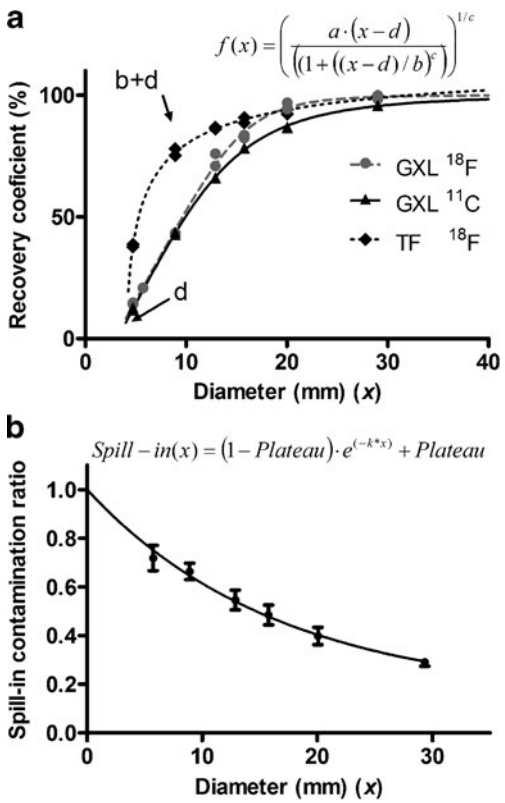

Fig. 1 The static arterial phantom was used to obtain the recovery factors for cylindrical objects (syringes) ranging in diameter from 4 to 29 mm (**a**) and equations to calculate the spill-in ratio (**b**). **a** The phantom was imaged on the Philips Gemini TF PET/CT scanner with ^{18}F (*dashed line*, *diamonds*) and on the Gemini GXL PET/CT scanner with ^{11}C (*solid line*, *triangles*) and with ^{18}F (*dotted line*, *circles*). These data were then fitted using Eq. 1, and the fits are represented by the curves. **b** Symbols represent a series of activities and the exponential fit to the data

The parameters a and d in Eq. 1 represent, respectively, the slope of the curve and the lower limit of the object's diameter which may be corrected adequately. The artery dimensions obtained from CT images were the same as the object dimensions. Therefore the value could be directly used. However, the relationship between the full-width at half-maximum (FWHM) of the object measured on the PET images and the actual size of the target (syringe diameter) was evaluated using a second-order polynomial fit (quadratic equation) (Fig. 2):

$$f(x) = B_0 + B_1 x + B_2 x^2 \quad (2)$$

The second aim was to accurately determining the spill-in correction factor as a function of object diameter (Fig. 1b). Contamination from outside the syringe represents spill-in at an exponential rate into the lumen as a function of the diameter. ROIs were drawn on the transaxial plane of each syringe and the average results were fitted to Eq. 3 for the spill-in factor of the object diameter (Fig. 1b).

$$Spill-in(x) = (1-Plateau)\cdot e^{(-k^*x)} + Plateau \quad (3)$$

The monoexponential equation is described with k, a constant equal to the reciprocal of the spill-in range, the object diameter x, and Plateau corresponding to the asymptotic spill-in contribution to very large objects.

Most of the phantoms used to image arteries have a diameter of 6.35 mm to simulate a carotid artery and 6.35 mm or 7.94 mm for a superficial femoral artery [27]. In the present study, we used a diameter of 6.35 mm to represent the diameters of both the carotid and femoral arteries. This was based on reported values measured by CT, Doppler, pathological examination and MRI, in which the diameter of these arteries ranged from 4.4 to 12 mm, with a mean diameter of 7 mm [27–30]. It is, however, important to keep

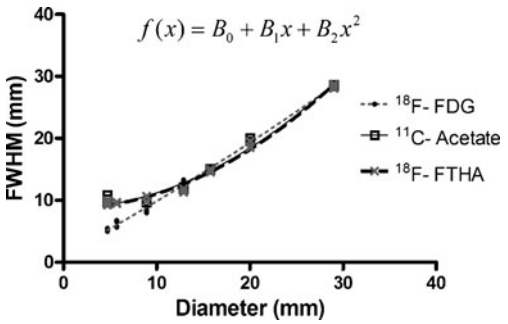

Fig. 2 Correlation between FWHM measured in the PET images using an activity profile across the centre of the syringes and the actual diameter of the static arterial phantom syringes. Lines represent the fits: for the ^{18}F-FDG brain imaging protocol with 2-mm voxels on the Gemini TF PET/CT scanner (*dotted line*, *circles*), and for ^{11}C-acetate (*solid line*, *squares*) and ^{18}F-FTHA with a whole-body protocol and 4-mm voxels on the Gemini GXL PET/CT scanner (*dashed line*, *crosses*)

in mind that artery diameter varies from person to person according to factors such as age, sex, and weight [31].

For our three imaging protocols, we set blood flow in the dynamic phantom to 200 ml/min for both the femoral and the carotid arteries. This rate compares well with the actual flow rate reported for the superficial femoral artery (196± 65 ml/min) [32] and carotid artery (251±51 ml/min) [33]. This was done with a phantom designed to simulate arterial blood flow in muscle. The phantom consisted of Tygon tubing immersed in a water bath representing the muscle surrounding the artery. One end of the tube was attached to a reservoir that was used to introduce and modulate the concentration of radiotracer. Blood circulation was simulated by pumping water at a constant rate of 200 ml/min through the field of view of the PET scanner. To model blood flow following bolus injection, we started with an initial volume of 400 ml of water in the reservoir and then poured 200 ml of radiotracer solution into the reservoir over a period of 1 min. Water was then added to the reservoir at a rate of 400 ml/min to represent the blood clearance of the radiotracer. Samples were taken from the reservoir at 20 s, 40 s, 60 s, 2 min, 3 min, 5 min and 10 min to simulate blood sampling in patients, and their radioactivity was measured in a gamma counter (Cobra). Since this is considered to be equivalent to performing blood sampling in a patient, it was our gold standard for phantom measurements (Fig. 3a).

The radioactivity in the simulated blood samples taken from the reservoir was expressed in kBq/ml and was correlated with the IDIF derived from PET imaging of the dynamic phantom after proper correction for RCs. Three transaxial ROIs were drawn on adjacent axial planes and the maximum value of the four highest adjacent pixels was recorded. The maximum concentration of radiotracer in the carotid phantom (20–40 kBq/ml) was similar to that administered to subjects during our clinical studies. In order to establish the reliability of the FWHM correction method under different conditions, the arterial injection modelling experiments were repeated three times for each protocol.

Human studies

The data for the present analysis came from two different clinical research projects that took place in our PET facility. One was a dynamic analysis of femoral muscle metabolism in diabetic patients and the other was an evaluation of brain glucose metabolism in young and elderly subjects. In the first study, six healthy volunteers, all men aged 37± 13 years, were imaged first with 185 MBq of ^{11}C-acetate for 30 min in dynamic list mode and then with 185 MBq of the fatty acid analogue ^{18}F-FTHA for another 50 min, again using dynamic list mode acquisition. This study was done on a Philips Gemini GXL PET scanner using a row action

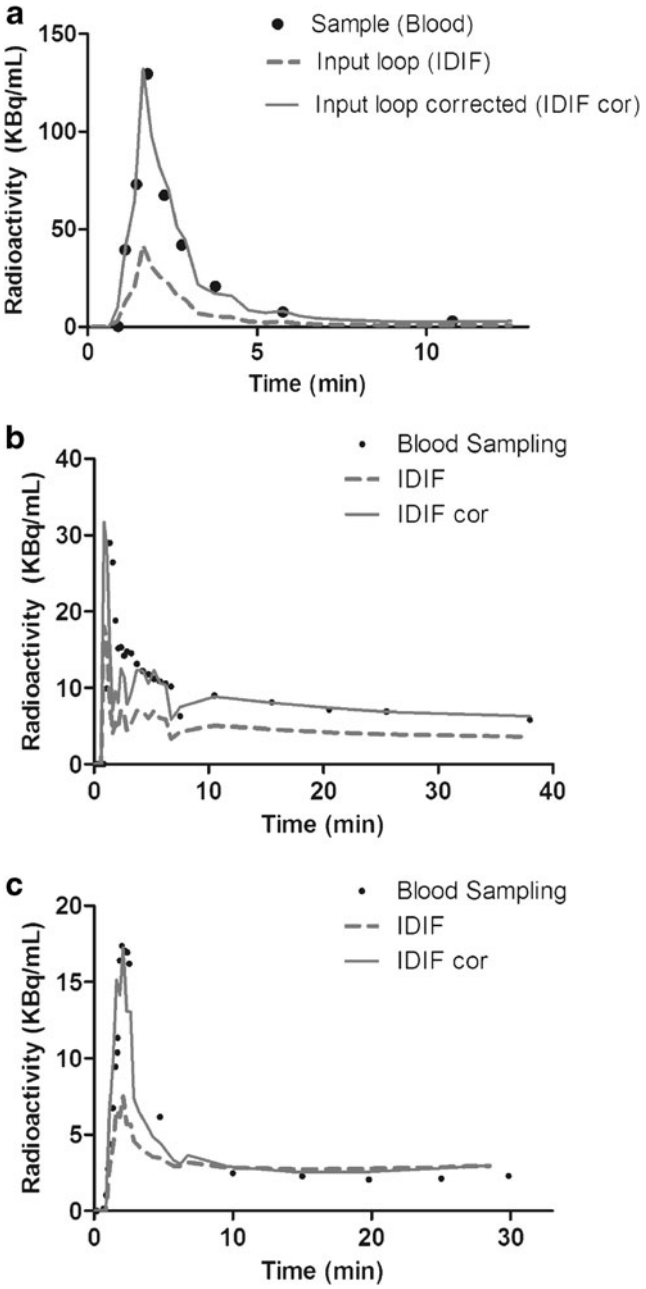

Fig. 3 Time–activity curves of input functions from withdrawn blood samples and the IDIF with the appropriate correction. **a** Dynamic artery phantom designed to model radiotracer influx and blood clearance. The phantom was made from Tygon tubing, 6.35 mm diameter, entering the PET scanner field of view and attached to a water reservoir used to introduce the radiotracer into the system. Samples taken from the phantom (*solid circles*) were used as reference and were compared to data obtained from uncorrected IDIF (*dashed line*) and the IDIF-corrected for partial volume using the corresponding diameter estimated from the FWHM (*solid line*). **b**, **c** Examples of input function for a ^{18}F-FDG brain study and for a ^{18}F-FTHA muscle study (*solid circles* blood samples, *dashed line* IDIF not corrected. *solid line* IDIF corrected)

maximum likelihood algorithm (RAMLA) without sinogram rebinning for reconstructing images and a time sequence of 12×15 s, 8×30 s, and 3×60 s, with the remaining acquisitions being reconstructed with 5-min time frames. The other parameters were as follows: isotropic voxel size 4 mm, and 60-cm diameter by 18-cm axial field of view. All IDIF and the FWHM were drawn on both the left and right arteries over three consecutive planes, with 4 cm between planes. The maximum value of the four highest adjacent pixels for each frame were recorded.

In the second study, the cerebral metabolic rate of glucose (CMRglc) was measured with ^{18}F-FDG in six healthy volunteers, five men and one woman aged 59± 23 years. These scans were performed on a Philips Gemini TF scanner using list mode, with time-of-flight enabled, with the same time frames and parameters as the first study except for the image reconstruction algorithm (line-of-response row action maximum likelihood algorithm) and the size of the isotropic voxel which was 2 mm. For the carotid arteries, the ROIs were drawn from the PET/CT coregistration images. For each artery, three adjacent planes were selected below the skull, their x and y diameter was then measured from the CT images and the maximum value of the four highest adjacent pixels for each plane was recorded. Serial blood sampling was done in both studies following the same time points as the dynamic sequence (12×15 s, 8×30 s, 3×60 s, and all subsequent samples withdrawn every 5 min). The arterialized venous blood was withdrawn with retrograde insertion of a cannula into a dorsal arm or a distal forearm vein. The limb was kept warm with a heating blanket.

PET data analysis

In the first study, the muscle perfusion index K_1 (min^{-1}) was estimated from ^{11}C-acetate using a three-compartment model [11, 34]:

$$C_t(t) = [A_1 \cdot \exp(-(k_2 + k_3)t) + A_2 \cdot \exp(-k_4 t)] \otimes C_p(t) + v.C_{tot}(t) \quad (4)$$

$$A_1 = K_1 k_2/(k_2 + k_3)$$

$$A_2 = K_1 k_3/(k_2 + k_3)$$

In Eq. 4, C_t, C_p and C_{tot} represent as a function of time the tracer concentration in tissue, plasma and the total arterial blood, respectively. K_1 to k_4 are the rate constants and v represents the blood volume. In this equation, K_1 represents blood flow, while k_2 is an index of myocardial oxygen consumption.

The contribution of ^{11}C-acetate metabolites to the radioactivity measured in the plasma was estimated as follows:

$$C_p(t) = [1 - a_o \cdot (1 - \exp(-t \cdot \log 2/m))] \cdot C_{tot}(t) \quad (5)$$

In Eq. 5, the variables a_o and m are the parameters to be fitted.

For the ^{18}F-FTHA data, in order to compare the IDIF obtained from the ROIs with those obtained from the actual plasma samples taken from the subjects (Fig. 5), we corrected first for the PVE (Eq. 1) corresponding to the artery diameter estimated from the FWHM of the radioactivity profile. After that, a second correction was applied for the spill-in of radioactivity from muscle into the artery lumen in the late portion of the time–activity curve (TAC). This was done again with the corresponding factor for the diameter observed (Fig. 1b), multiplied by each point of the muscle activity and subtracted from the TAC where the activity of the muscle in the late portion was higher or equal to the artery lumen (Fig. 3b). This approach of spill-in correction was compared with another technique in which a blood sample is needed. This was done by subtracting the value of the last point of the ROI TAC from the corresponding blood sample radioactivity, thereby obtaining the amount of unwanted radioactivity coming from muscle tissue. This value was then divided by the muscle radioactivity content estimated from the PET image, with the resulting fractional factor then being used to correct the late portion of the TAC [35]. Both approaches yielded similar results (r^2=0.99 Fig. 5d). Lastly, the data were corrected for the presence of ^{18}F-FTHA metabolites in the blood. To comply with our kinetic model, the quantitative (kBq/ml) values were obtained for whole blood and converted to plasma values using a constant factor derived from the subject's blood samples. With these corrections, the plasma to tissue transfer rate, K_i, was obtained using a Patlak graphical analysis for irreversible ligands (Eq. 6) [14, 36]:

$$K_i = \frac{K_1 \cdot k_3}{k_2 + k_3} \quad (6)$$

The transfer of the tracer from plasma to the irreversible compartment (K_i) was estimated from Eq. 7:

$$\frac{C_t(t)}{C_p(t)} = K_i \frac{\int_0^T C_p(t)dt}{C_p(t)} + V_d \quad (7)$$

Because Eq. 7 is linear at equilibrium (5–35 min) [37], the fractional uptake constant (K_i) can be derived directly

from the slope of the curve of $C_t(T)/C_p(T)$ against $C_p(T)$ divided by the integral of the plasma TAC-$C_p(T)$.

In the second study, we used the classical three-compartment model (Eq. 8) to estimate CMRglc as originally described by Sokoloff et al. [37], a method which has been validated for ^{18}F-FDG studies in the human brain [13].

$$CMRglc = \frac{C_p}{LC} \cdot \frac{K_1 \cdot k_2}{k_2 + k_3} \quad (8)$$

where CMRglc is in milligrams per 100 g per minute, C_p is the plasma glucose concentration, LC is a lumped constant (0.52) [38], k_1 and k_2 are the rate constants for carrier-mediated transport of ^{18}F-FDG between plasma and tissue and k_3 is the phosphorylation rate constant of ^{18}F-FDG at steady-state. The IDIF were only corrected for the partial volume. Correction for spill-in was not necessary as the carotid ROIs are located outside of the skull where they are not contaminated by radioactivity from the brain [23]. We used a large ROI, for the brain tissue, traced on the frontal lobe of the brain without using a morphological atlas to estimate CMRglc.

Statistical analysis

All data were expressed as means±SD. Pearson correlation coefficients (r) and the determination coefficients (r^2) were used to evaluate the strength of the relationship between the diameter of the arterial phantom syringes, the FWHM obtained by PET and artery dimensions obtained by CT. For the human studies, the Pearson correlation and determination coefficients were used to assess the relationship between the IDIF, spill-in factor correction, Tygon tubing size, measurements obtained from the subjects and phantom blood clearance curves. For the brain study, arterial dimension and FWHM from the PET activity profiles were compared using a paired t-test. One-way repeated measures (ANOVA) with Tukey's test was used to assess the differences between the blood sampling data, the IDIF not corrected for PVEs and the IDIF corrected for PVEs in the clinical studies. All p values smaller or equal to 0.05 were considered statistically significant.

Results

The RC curves for each type of study and scanner from the phantom measurements are shown in Fig. 1. To define our correction domain, we set the upper limit for the RC at 90%, while the lower limit below which the correction is a constant factor, was set by the value of d in Eq. 1. We also measured the relationship between the FWHM obtained from PET images and the true diameter of the targets. This relationship between the PET-derived FWHM and actual phantom syringe size was needed, since without contrast agents it was not possible to reliably measure the diameter of the superficial femoral artery directly using the CT images from the PET/CT scanner in this study. Fitting the data from the phantom to a second-order polynomial equation showed a highly significant correlation (r^2>0.98) between the PET-measured FWHM and the real diameter of the simulated arteries. With a regression curve, the standard deviation of the residuals (S_{xy}) was 0.9 mm for ^{11}C-acetate, 0.6 mm for ^{18}F-FTHA and 0.5 mm for ^{18}F-FDG (Fig. 2).

Further validation of the second-order polynomial equation fitted model was obtained from the 6.35-mm inner diameter tube of the dynamic femoral phantom. All validations were done in triplicate for each scanner and study condition (Table 1). ^{11}C-Acetate overestimated the size of the target (6.35 mm tubing) by 6±2%, while underestimation with ^{18}F-FTHA was less (3±2%). For the brain study with ^{18}F-FDG on the Gemini TF, the carotid artery diameter was slightly overestimated (4±7%) and the data were more variable.

For the brain study, the diameter of the left and right median carotid arteries was estimated from the PET image following a ^{18}F-FDG bolus injection. From the coregistered PET/CT image, it was also possible to locate the arteries on the CT image and measure their diameter. The measured values were not significantly different: 7.3±0.6 mm by PET and 7.9±0.5 mm by CT (paired Student's t-test; p=0.08). Consequently, there were no significant differences between the RCs extracted using the PET or the CT images (0.54±0.04 vs. 0.58±0.03; p=0.24). Thus there was a nonsignificant difference between the values of CMRglc (14.0±5.7 vs 13.4±5.6; p=0.18) obtained using the two artery size measurement methods.

The dynamic femoral phantom was designed to simulate the influx and subsequent clearance of a bolus injection of radiotracer in an artery (Fig. 3a), as well as to model the blood clearance curve. Here also, all measurements were performed in triplicate for each protocol. The radioactivity data obtained from sampling the radioactive solution in the phantom reservoir were first converted into kBq/ml and then correlated with the phantom PET data, corrected for the PVE using RCs corresponding to the tube inner diameter of 6.35 mm. The following coefficients of determination (r^2) were obtained: Gemini GXL with whole-body protocol for ^{11}C-acetate and ^{18}F-FTHA r^2=0.94 and 0.99, respectively, and Gemini TF with brain study protocol for ^{18}F-FDG r^2=0.98.

The correction methods developed with the phantoms were then applied to actual human subject data. With ^{11}C-acetate, the perfusion index, K_1 (min^{-1}), was obtained independently for both the vastus lateralis and the biceps femoris muscles using a three-compartment model (Fig. 4). The perfusion

Table 1 Recovery coefficients and the corresponding diameters (means±SD) estimated from the FWHM measured in the PET images

Radiotracer		Diameter (mm)	Recovery coefficient	r^2 value[c]
^{18}F-FDG (Gemini TF)	Human carotid[a]	7.93±0.46	0.58±0.02	
	Phantom[b]	6.65±0.44	0.49±0.03	0.975
^{11}C-acetate (Gemini GXL)	Human femoral artery[a]	9.63±0.78	0.52±0.08	
	Phantom[b]	6.77±0.12	0.28±0.01	0.940
^{18}F-FTHA (Gemini GXL)	Human femoral artery[a]	9.48±1.21	0.49±0.09	
	Phantom[b]	6.21±0.13	0.25±0.01	0.990

[a] Human studies (n=6).

[b] Dynamic phantom (tube diameter 6.35 mm) (n=3).

[c] Correlation of the IDIF with the radioactivity of the samples from the phantom reservoir.

index for both muscles was not significantly different when estimated from the blood TAC (0.34±0.18 min^{-1}) compared to the corrected IDIF (0.29±0.15 min^{-1}). However, the uncorrected IDIF gave perfusion index values of 0.66± 0.41 min^{-1} that were significantly overestimated compared to those obtained from the blood TAC or with the corrected IDIF repeated measures ANOVA (p<0.0001).

For the ^{18}F-FTHA study, the muscle (vastus lateralis, biceps femoris) to plasma transfer rate constant (K_i) was computed from a Patlak graphical analysis (Fig. 5), yielding the following values: AIF from the plasma samples (K_i=0.076±0.035 min^{-1}), IDIF corrected for the PVE and the spillover from the muscle (K_i=0.074±0.031 min^{-1}) and uncorrected IDIF (K_i=0.102±0.044 min^{-1}). There was a significant positive correlation (r=0.86, p=0.027, for vastus lateralis; r=0.89, p=0.017, for biceps femoris) between the slopes of the corrected data and the actual plasma radioactivity AIF. However, there was no correlation (r=0.04 for vastus lateralis, and r=0.002 for biceps femoris) between the slopes of the Patlak curves derived from the AIF and the uncorrected IDIF.

In the ^{18}F-FDG brain imaging study, a standard compartmental analysis was applied using the frontal brain region for the tissue, and the blood curve was obtained using blood samples, the uncorrected IDIF and the IDIF corrected for PVE (Fig. 6). For blood samples, IDIF without correction and the IDIF corrected for PVE the K_1 values were 0.029±0.011 min^{-1}, 0.076±0.014 min^{-1} and 0.039±0.007 min^{-1}, respectively. The average CMRglc values for the frontal brain were obtained from each input function: blood samples 13.8±3.9 mg/100 g per minute, IDIF without correction 24.8±8.8 mg/100 g per minute and IDIF corrected for PVE 14.0±5.7 mg/100 g per minute. Thus, omitting the correction for PVE resulted in an overestimation of the CMRglc by a factor of approximately two. One-way ANOVA repeated measures and Tukey's test showed significant differences for K_1 and CMRglc only for the IDIF uncorrected for PVE (F(2,5)=48.37; p<0.0001) and (F(2,5)=36.42; p<0.0001).

In order to establish the robustness of the correction when applied to human studies, we assessed the impact of corrections for PVEs assuming differences of ±1 mm between the real and measured artery sizes. For the ^{11}C-acetate muscle study, underestimating the femoral artery size by 1 mm resulted in an underestimation of the perfusion index by 67±6%; if the size was overestimated by 1 mm, the perfusion index was overestimated by 66±9%. A similar but less important effect was observed with ^{18}F-FTHA where the effect on the K_i for a 1-mm underestimation and overestimation was −13±6% and +12±6%, respectively. Although a ±1-mm error is unlikely with the CT modality because of its excellent spatial resolution, we were nonetheless interested in computing the effect of such a deviation on the estimation of CMRglc by CT. It was found that an underestimation of the diameter of the carotid artery by 1 mm would decrease CMRglc by 17±6% whereas an overestimation by 1 mm would increase it by 10±3%.

Discussion

We report here two specific developments: (1) methods for PVE correction appropriate for the PET camera, isotopes, acquisition protocols and kinetic reconstruction, and (2) an excellent correlation between AIF and IDIF obtained in the same subjects, based on the results of experiments conducted using a static phantom to measure RCs for blood vessels of various sizes and a dynamic phantom aimed at modelling the AIF. We already know that kinetic analysis yields important information that cannot be obtained from static images. In cardiac imaging, for example, kinetic analysis of ^{11}C-acetate PET data is useful to measure myocardial perfusion and oxygen consumption [39, 40]. Similarly, CMRglc can only be obtained using tracer kinetic analysis [8]. One of the main limitations of kinetic analyses is the necessity to draw serial arterial or arterialized blood samples to obtain the blood input function required by the mathematical models [1]. Other strategies

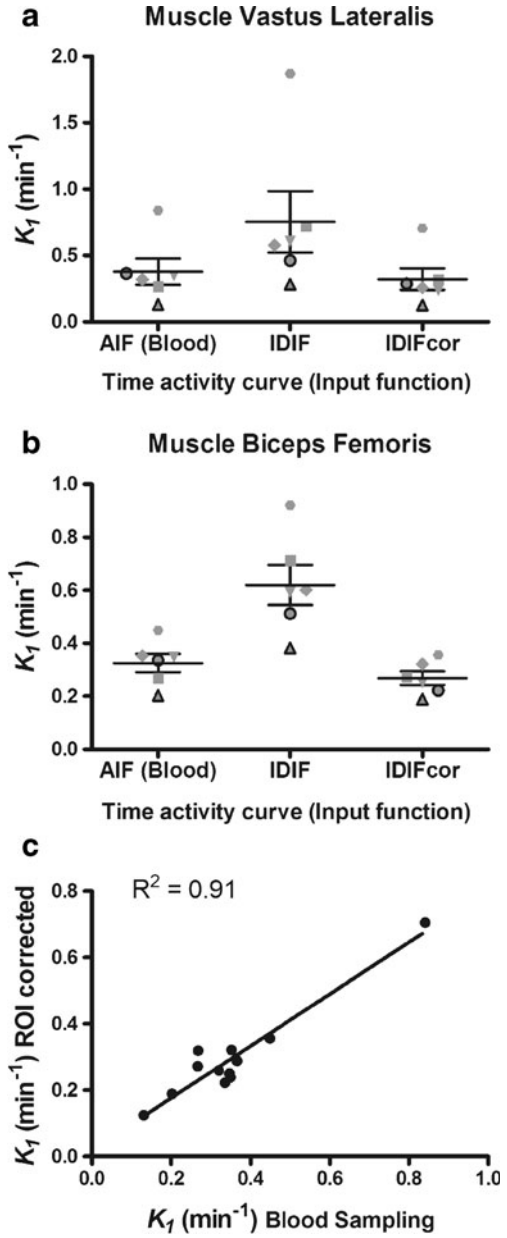

Fig. 4 **a**, **b** ^{11}C-acetate perfusion index, K_1, for the vastus lateralis (**a**) and biceps femoris (**b**) obtained by kinetic analysis with a three-compartment model. For each muscle, the average and range of K_1 values were obtained from an AIF derived by blood sampling (*Blood*), IDIF and corrected for PVE (*IDIFcor*). **c** The K_1 values obtained from blood sampling are also correlated with the corrected IDIF values. The data from each subject are identified by the same symbol across all conditions

exist to bypass this requirement [8, 19–23], but the use of an IDIF is attractive for several reasons. First, it eliminates a common source of error – the need for precise cross-calibration between a dose calibrator and the PET scanner. Second, by providing the equivalent of an AIF without blood sampling during the acquisition, IDIF makes the study simpler, with reduced risk and discomfort for the subject, fewer manipulations, reduced personnel requirements, and lower risk of occupational hazards related to blood handling. Third, serial blood sampling can also be a deterrent to subject participation when venous or arterial access is problematic, i.e. in cancer patients or in the elderly.

Despite its intrinsic utility, IDIF has some limitations. The first is the need to correct for PVEs. Because of the difficulty in obtaining reliable data from arterial imaging, IDIF was for a long time restricted to the left ventricle, which offers a relatively large pool of arterial blood in myocardial imaging studies [36]. Now that most human PET/CT scanners can achieve a spatial resolution <5 mm, IDIF analysis can be considered for large blood vessels such as the femoral or the carotid arteries [23]. Accurate determination of the diameter of large arteries by PET/CT allows the computation of reliable recovery factors, making it possible to obtain the equivalent of AIFs directly from the ROIs traced on the PET/CT images of these arteries. The availability of more sensitive scanners and the feasibility of using list mode along with better reconstruction algorithms have also contributed to the improvement in spatial and time resolution, and thus to the quality of radiotracer kinetic analysis.

PVE is also a key challenge in obtaining an accurate IDIF. In 1984, Kessler et al. [41] were among the first to propose a correction scheme for PVE which took into account the impact of the physical characteristics of the scanner. In the present study, emphasis was placed on the reconstructed image, since the scanner characteristics, the nature of the radiotracer and blood vessel diameter are implicitly present in the data derived from the image. Accordingly, the mathematical expressions we used to correct for PVE were directly derived from the images obtained in each study, making it easier to integrate the scanner characteristics while computing the recovery factors.

When dealing with recovery factors, the behaviour of cylindrical objects such as arteries is quite different from that of spherical objects, since shape has an effect on voxel overlap [42]. Thus, a cylindrical phantom was selected instead of the usual spherical ones to properly simulate blood vessel geometry. In this study, phantom measurements confirmed that the combination of CT and PET images within the same investigation can improve the measurement of target size and spatial position compared to conventional PET without CT.

Once the proper artery diameter was established, the data from the dynamic PET acquisition were validated against the water reservoir samples. Each protocol was evaluated, since ^{11}C has a longer positron range than ^{18}F, and we believe this explains why the size estimate was less precise with this isotope. The FDG study was performed using a different scanner (Gemini TF instead of Gemini GXL), with a higher spatial resolution and smaller voxels for the brain acquisition protocol. This explains why the size estimate was more precise with ^{18}F-FDG than with ^{18}F-FTHA.

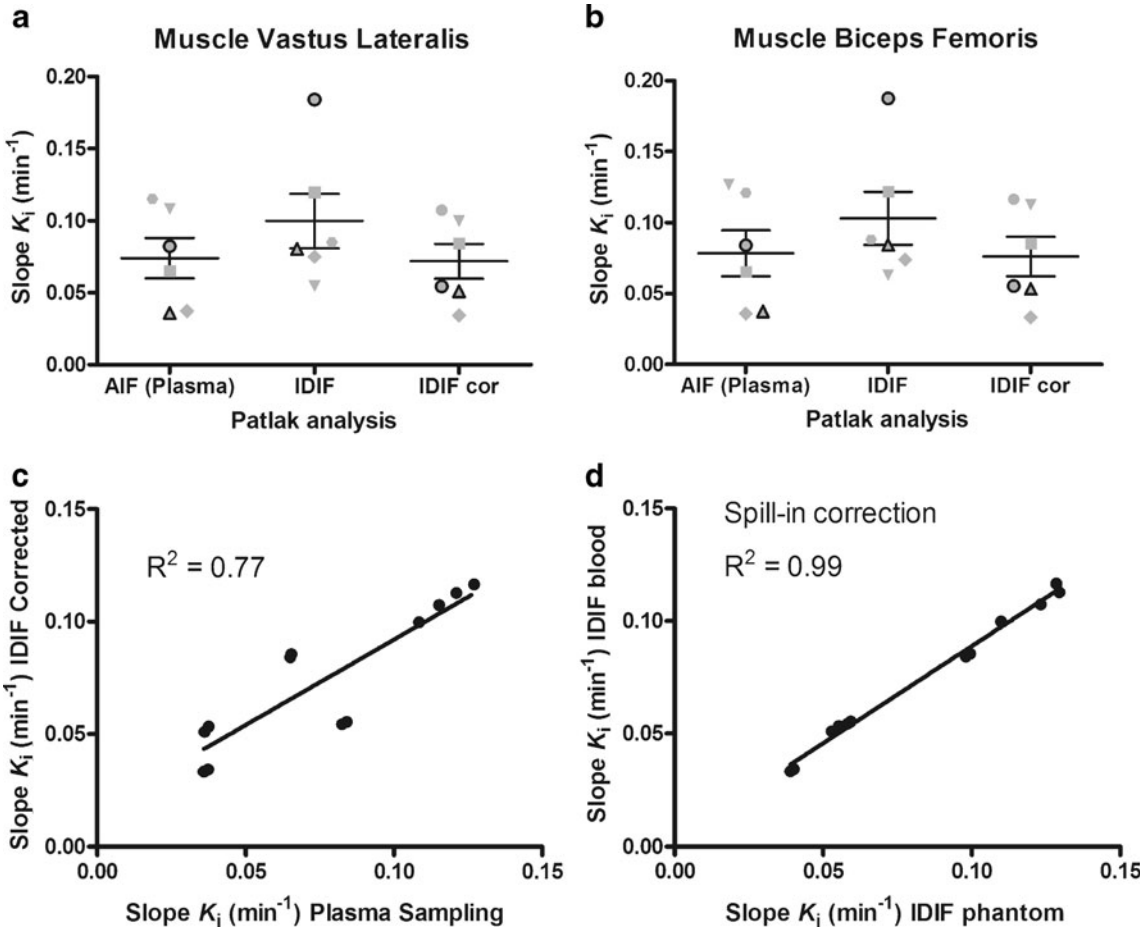

Fig. 5 **a**, **b** Slope of the plasma to tissue transfer rate, K_i (min^{-1}), of ^{18}F–FTHA for the vastus lateralis (**a**) and biceps femoris (**b**) obtained by Patlak graphical analysis. For each muscle, the average and range of K_i was obtained from an AIF derived from blood sampling (*Plasma*), uncorrected IDIF and corrected for PVE and spillover (*IDIF cor*). The data from each patient are identified by the same symbol across all conditions. **c** The K_i values obtained from blood sampling are correlated with the corrected IDIF values. **d** The values of K_i measured using IDIF corrected for spill-in with the late blood sample are correlated with the K_i measured using IDIF corrected for spill-in with the static phantom-derived function

Blood sampling is widely considered to be the gold standard for AIF, but blood samples are almost exclusively taken from the extremity of the upper limbs. This means that the sampling site is often quite remote from the target organ, requiring the assumption that the blood tracer concentration within the arterial network is homogeneous. However, when the AIF is obtained by IDIF, a blood vessel close to the target organ can be selected, which is more representative of the true tracer input to the target organ.

Nevertheless, the IDIF obtained from PET data represents whole blood activity and a partition coefficient must be assumed to provide the plasma input function. There is now, however, a tendency to prefer whole blood to calculate the AIF, as this makes the experiment simpler and also yields reliable results [43]. Since the clinical studies were at the pilot stage, our analysis was not powered to detect substantial differences between the various blood analysis methods. The fact that we did detect a substantial difference between the uncorrected IDIF and the blood samples shows that proper correction methods must be applied to the image-derived AIF. While we observed a good general agreement between the values provided by corrected IDIF and blood samples, further studies are needed on larger datasets to properly document the error of the estimate provided by the use of a corrected IDIF compared to blood samples.

The kinetic model used for our ^{11}C-acetate PET measurements of heart oxygen consumption already has IDIF built into the study design in which the AIF came from ROIs traced on the left ventricular cavity. In this model, a whole-blood input function is used instead of plasma sampling [26, 40]. For ^{11}C-acetate kinetics with high blood flow rates, it may be appropriate to use a first pass extraction model [44], but considering that we were concerned with validating AIFs from ROIs traced on leg arteries at rest which have a low perfusion rate, our current model was assumed to be appropriate. Measurements

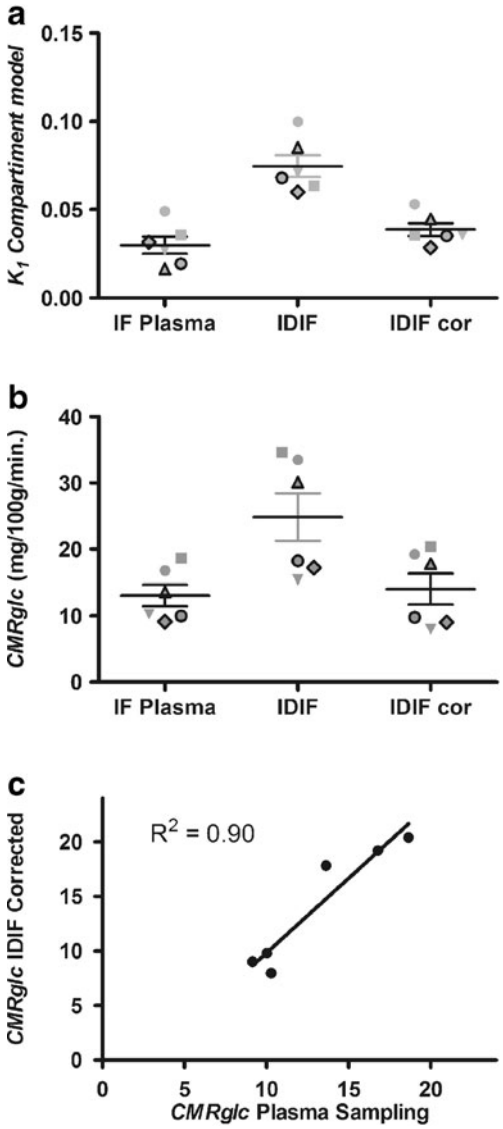

Fig. 6 CMRglc from standard three-compartment model analyses of ^{18}F-FDG dynamic brain imaging, using an ROI on the frontal lobe of the brain. **a** The K_1 fit from the compartmental model was computed using three different input functions: plasma sampling (*Plasma*), IDIF without correction, and IDIF corrected for carotid artery PVE (*IDIF cor*). **b** CMRglc was computed using three different input functions: plasma sampling (*Plasma*), IDIF without correction, and IDIF corrected for carotid artery partial volume (*IDIF cor*). For each subject, the diameter of the carotid artery was obtained from the bolus PET/CT coregistration images by measuring artery size on the CT image. The data from each patient are identified by the same symbol across all conditions. **c** Correlation between CMRglc of the frontal brain region derived from plasma sampling and from IDIF corrected for PVE

performed with ^{13}C-acetate have shown that the average uptake of acetate for the leg muscle at rest is 15 μmol min^{-1}, with a release rate of 5 μmol min^{-1}, which accounts for 4% and 1.5% of the available acetate, respectively [45]. These results make it likely that enough ^{11}C-acetate reaches the leg muscle to correctly measure its perfusion index even at rest.

For the analysis of ^{18}F-FTHA uptake in the femoral muscle, we chose Patlak graphical analysis. Maki et al. [36] did a 30-min heart acquisition followed by a 15-min acquisition in the leg muscle. Plasma was collected throughout the study and corrected for the presence of metabolites. To obtain the IDIF in our study, we first measured whole blood values from the images, corrected them for PVE, then for the spill-in, for the presence of ^{18}F-FTHA metabolites and finally derived plasma values from whole blood. Although the protocol for the femoral muscle ^{11}C-acetate and brain ^{18}F-FDG study did not require the sampling of blood during the acquisition procedure, with ^{18}F-FTHA, blood samples have to be collected for the metabolites. The ^{18}F-FTHA data were fitted to a one-phase exponential decay to correct the IDIF. Nevertheless in the long run, we aim to reduce or even completely eliminate the need for blood sampling during ^{18}F-FTHA acquisition. However, since all of our data came from patients in whom the circulating glucose level was kept constant with a euglycaemic-hyperglycaemic clamp, further experiments will have to be conducted in normal subjects before we can presume universality of this method. We found that uncorrected IDIF scores were inconsistent, but that correcting for the recovery factor significantly reduced data variability and yielded a good correlation (r^2=0.78) between the results calculated using the IDIF and actual AIF. These results emphasize the importance of properly correcting IDIF before using it for further analysis.

Data based on ^{18}F-FDG standardized uptake value or kinetic models are widely used in basic and clinical research [1, 5, 8, 9]. When performing IDIF studies with ^{18}F-FDG, the difference between concentrations of ^{18}F-FDG in whole blood and plasma can be ignored as it has been shown to have little or no impact on the final results [8]. Many studies have been conducted to eliminate the need for serial blood sampling [4, 8, 9, 17] during image acquisition, but most methods still require at least one blood sample to calibrate the input curve with the blood radioactivity concentration. Chen et al., for example, used a combination of blood samples and independent component analysis to obtain the input function [20]. Mourik et al. found good agreement when using IDIF calibrated with a blood sample, but had poorer results when using an IDIF corrected with RCs, perhaps due to the method used to measure the RC [22]. A similar approach was used by de Geus-Oei et al. [46].

A major challenge in measuring IDIF is to obtain a proper recovery factor for the reference artery. To assess the robustness of our method for measuring arterial diameter, we computed the impact of an error of ±1 mm on the IDIF values. Even with a 1-mm deviation, the derived IDIF value remained closer to the true AIF derived from blood sampling as compared to an uncorrected IDIF value.

Considering that we used the mean of six ROIs for the femoral arteries, it is very unlikely that an error as large as 1 mm would have occurred; such an error exceeds our experimental variability with the CT measurement which was of the order of 0.5 mm for the carotid artery. With ^{18}F-FDG, PET/CT could be used to obtain the diameter of the artery from the coregistered CT and ^{18}F-FDG bolus PET images. These images make it easy to correct the data for PVE, an important advantage of this approach.

Conclusion

The use of PET/CT imaging with correction for spillover and PVE allows precise determination of blood radiotracer concentration in major vessels and makes it possible to extract accurate quantitative kinetic data using an IDIF. As a result, we showed that blood sampling can be avoided during the acquisition while simultaneously obtaining a precise and accurate AIF. The proposed method requires precise phantom measurements of RCs and accurate determination of artery diameter, which are procedures well within the capability of most PET imaging facilities involved in clinical research.

Acknowledgments This work was supported by the Canadian Institutes of Health Research (CIHR-MOP53094 and PRG-80137), a postgraduate scholarship from the Natural Sciences and Engineering Research Council of Canada (E.C.), the Canada Research Chairs Secretariat, scholarships from the Canadian Foundation for Innovation and Fonds de la recherche en santé du Québec (F.B., A.C.C.), and a doctoral award from the Canadian Diabetes Association (S.M.L.). The Centre de recherche clinique Etienne-Le Bel is a FRSQ-funded research center.

References

1. Logan J, Alexoff D, Kriplani A. Simplifications in analyzing positron emission tomography data: effects on outcome measures. Nucl Med Biol 2007;34:743–56.
2. van der Weerdt AP, Klein LJ, Boellaard R, Visser CA, Visser FC, Lammertsma AA. Image-derived input functions for determination of MRGlu in cardiac (18)F-FDG PET scans. J Nucl Med 2001;42:1622–9.
3. Wu HM, Hoh CK, Choi Y, et al. Factor analysis for extraction of blood time-activity curves in dynamic FDG-PET studies. J Nucl Med 1995;36:1714–22.
4. Phillips RL, Chen CY, Wong DF, London ED. An improved method to calculate cerebral metabolic rates of glucose using PET. J Nucl Med 1995;36:1668–79.
5. Graham MM, Peterson LM, Hayward RM. Comparison of simplified quantitative analyses of FDG uptake. Nucl Med Biol 2000;27:647–55.
6. Huang SC. Anatomy of SUV. standardized uptake value. Nucl Med Biol 2000;27:643–6.
7. Ogden RT. Estimation of kinetic parameters in graphical analysis of PET imaging data. Stat Med 2003;22:3557–68.
8. Chen K, Bandy D, Reiman E, et al. Noninvasive quantification of the cerebral metabolic rate for glucose using positron emission tomography, 18F-fluoro-2-deoxyglucose, the Patlak method, and an image-derived input function. J Cereb Blood Flow Metab 1998;18:716–23.
9. Brock CS, Young H, Osman S, Luthra SK, Jones T, Price PM. Glucose metabolism in brain tumours can be estimated using [18F]2-fluorodeoxyglucose positron emission tomography and a population-derived input function scaled using a single arterialised venous blood sample. Int J Oncol 2005;26:1377–83.
10. Brun E, Kjellen E, Tennvall J, et al. FDG PET studies during treatment: prediction of therapy outcome in head and neck squamous cell carcinoma. Head Neck 2002;24:127–35.
11. Bentourkia M, Croteau E, Langlois R, et al. Cardiac studies in rats with 11C-acetate and PET: a comparison with 13N-ammonia. IEEE Trans Nucl Sci 2002;49:2322–7.
12. Maki MT, Haaparanta M, Nuutila P, et al. Free fatty acid uptake in the myocardium and skeletal muscle using fluorine-18-fluoro-6-thia-heptadecanoic acid. J Nucl Med 1998;39:1320–7.
13. Phelps ME, Huang SC, Hoffman EJ, Selin C, Sokoloff L, Kuhl DE. Tomographic measurement of local cerebral glucose metabolic rate in humans with (F-18)2-fluoro-2-deoxy-D-glucose: validation of method. Ann Neurol 1979;6:371–88.
14. Logan J. Graphical analysis of PET data applied to reversible and irreversible tracers. Nucl Med Biol 2000;27:661–70.
15. van der Weerdt AP, Klein LJ, Visser CA, Visser FC, Lammertsma AA. Use of arterialised venous instead of arterial blood for measurement of myocardial glucose metabolism during euglycaemic-hyperinsulinaemic clamping. Eur J Nucl Med Mol Imaging 2002;29:663–9.
16. Syvanen S, Blomquist G, Appel L, Hammarlund-Udenaes M, Langstrom B, Bergstrom M. Predicting brain concentrations of drug using positron emission tomography and venous input: modeling of arterial-venous concentration differences. Eur J Clin Pharmacol 2006;62:839–48.
17. Meyer PT, Circiumaru V, Cardi CA, Thomas DH, Bal H, Acton PD. Simplified quantification of small animal [18F]FDG PET studies using a standard arterial input function. Eur J Nucl Med Mol Imaging 2006;33:948–54.
18. Laforest R, Sharp TL, Engelbach JA, et al. Measurement of input functions in rodents: challenges and solutions. Nucl Med Biol 2005;32:679–85.
19. Litton JE, Hall H, Blomqvist G. Improved receptor analysis in PET using a priori information from in vitro binding assays. Phys Med Biol 1997;42:1653–60.
20. Chen K, Chen X, Renaut R, et al. Characterization of the image-derived carotid artery input function using independent component analysis for the quantitation of [18F] fluorodeoxyglucose positron emission tomography images. Phys Med Biol 2007;52:7055–71.
21. Su KH, Wu LC, Liu RS, Wang SJ, Chen JC. Quantification method in [18F]fluorodeoxyglucose brain positron emission tomography using independent component analysis. Nucl Med Commun 2005;26:995–1004.
22. Mourik JE, Lubberink M, Schuitemaker A, et al. Image-derived input functions for PET brain studies. Eur J Nucl Med Mol Imaging 2009;36:463–71.
23. Mourik JE, van Velden FH, Lubberink M, et al. Image derived input functions for dynamic high resolution research tomograph PET brain studies. Neuroimage. 2008;43:676–86.
24. Gregory R, Partridge M, Flower MA. Performance evaluation of the Philips "Gemini" PET. IEEE Trans Nucl Sci 2006;53:93–101.

25. Surti S, Kuhn A, Werner ME, Perkins AE, Kolthammer J, Karp JS. Performance of Philips Gemini TF PET/CT scanner with special consideration for its time-of-flight imaging capabilities. J Nucl Med 2007;48:471–80.
26. Prevost S, Lavallee E, Croteau E, et al. Partial volume effects on SUV measurements: impact of acquisition methods, reconstruction modes and image filtering for 2 dedicated PET scanners. J Nucl Med 2003;44:985.
27. Blake JR, Meagher S, Fraser KH, Easson WJ, Hoskins PR. A method to estimate wall shear rate with a clinical ultrasound scanner. Ultrasound Med Biol 2008;34:760–74.
28. Radegran G, Saltin B. Human femoral artery diameter in relation to knee extensor muscle mass, peak blood flow, and oxygen uptake. Am J Physiol Heart Circ Physiol 2000;278:H162–7.
29. Williams MA, Nicolaides AN. Predicting the normal dimensions of the internal and external carotid arteries from the diameter of the common carotid. Eur J Vasc Surg 1987;1:91–6.
30. Olufsen MS, Peskin CS, Kim WY, Pedersen EM, Nadim A, Larsen J. Numerical simulation and experimental validation of blood flow in arteries with structured-tree outflow conditions. Ann Biomed Eng 2000;28:1281–99.
31. Sandgren T, Sonesson B, Ahlgren R, Lanne T. The diameter of the common femoral artery in healthy human: influence of sex, age, and body size. J Vasc Surg 1999;29:503–10.
32. Hussain ST, Smith RE, Wood RF, Bland M. Observer variability in volumetric blood flow measurements in leg arteries using duplex ultrasound. Ultrasound Med Biol 1996;22:287–91.
33. Bartlett ES, Walters TD, Symons SP, Fox AJ. Carotid stenosis index revisited with direct CT angiography measurement of carotid arteries to quantify carotid stenosis. Stroke 2007;38:286–91.
34. Buck A, Wolpers HG, Hutchins GD, et al. Effect of carbon-11-acetate recirculation on estimates of myocardial oxygen consumption by PET. J Nucl Med 1991;32:1950–7.
35. Gambhir SS, Schwaiger M, Huang SC, et al. Simple noninvasive quantification method for measuring myocardial glucose utilization in humans employing positron emission tomography and fluorine-18 deoxyglucose. J Nucl Med 1989;30:359–66.
36. Maki MT, Haaparanta MT, Luotolahti MS, et al. Fatty acid uptake is preserved in chronically dysfunctional but viable myocardium. Am J Physiol 1997;273:H2473–80.
37. Sokoloff L, Reivich M, Kennedy C, et al. The [14C] deoxyglucose method for the measurement of local cerebral glucose utilization: theory, procedure, and normal values in the conscious and anesthetized albino rat. J Neurochem 1977;28:897–916.
38. Reivich M, Alavi A, Wolf A, et al. Glucose metabolic rate kinetic model parameter determination in humans: the lumped constants and rate constants for [18F]fluorodeoxyglucose and [11C]deoxyglucose. J Cereb Blood Flow Metab 1985;5:179–92.
39. Sun KT, Yeatman LA, Buxton DB, et al. Simultaneous measurement of myocardial oxygen consumption and blood flow using [1-carbon-11]acetate. J Nucl Med 1998;39:272–80.
40. van den Hoff J, Burchert W, Borner AR, et al. [1-(11)C]acetate as a quantitative perfusion tracer in myocardial PET. J Nucl Med 2001;42:1174–82.
41. Kessler RM, Ellis JR Jr, Eden M. Analysis of emission tomographic scan data: limitations imposed by resolution and background. J Comput Assist Tomogr 1984;8:514–22.
42. Soret M, Bacharach SL, Buvat I. Partial-volume effect in PET tumor imaging. J Nucl Med 2007;48:932–45.
43. Zanotti-Fregonara P, Maroy R, Comtat C, et al. Comparison of 3 methods of automated internal carotid segmentation in human brain PET studies: application to the estimation of arterial input function. J Nucl Med 2009;50:461–7.
44. Herrero P, Kim J, Sharp TL, et al. Assessment of myocardial blood flow using 15O-water and 1-11C-acetate in rats with small-animal PET. J Nucl Med 2006;47:477–85.
45. van Hall G, Sacchetti M, Radegran G. Whole body and leg acetate kinetics at rest, during exercise and recovery in humans. J Physiol (Lond) 2002;542:263–72.
46. de Geus-Oei LF, Visser EP, Krabbe PF, et al. Comparison of image-derived and arterial input functions for estimating the rate of glucose metabolism in therapy-monitoring 18F-FDG PET studies. J Nucl Med 2006;47:945–9.